

# Explaining wall-bounded turbulence through deep learning

A. Cremades<sup>a</sup>, S. Hoyas<sup>b</sup>, P. Quintero<sup>a</sup>, M. Lellep<sup>c</sup>, M. Linkmann<sup>d</sup>, R. Vinuesa<sup>e</sup>

<sup>a</sup>*CMT-Motores Térmicos, Universitat Politècnica de València, Camino de Vera s/n, Valencia, 46022, Spain*

<sup>b</sup>*Instituto Universitario de Matemática Pura y Aplicada, Universitat Politècnica de València, 46022 Valencia, Spain*

<sup>c</sup>*SUPA, School of Physics and Astronomy, The University of Edinburgh, James Clerk Maxwell Building, Peter Guthrie Tait Road, Edinburgh EH9 3FD, UK*

<sup>d</sup>*School of Mathematics and Maxwell Institute for Mathematical Sciences, University of Edinburgh, Edinburgh EH9 3FD, UK*

<sup>e</sup>*FLOW, Engineering Mechanics, KTH Royal Institute of Technology, SE-100 44 Stockholm, Sweden*

---

## Abstract

Despite its great scientific and technological importance, wall-bounded turbulence is an unresolved problem that requires new perspectives to be tackled. One of the key strategies has been to study interactions among the coherent structures in the flow. Such interactions are explored in this study for the first time using an explainable deep-learning method. The instantaneous velocity field in a turbulent channel is used to predict the velocity field in time through a convolutional neural network. The predicted flow is used to assess the importance of each structure for this prediction using a game-theoretic algorithm (SHapley Additive exPlanations). This work provides results in agreement with previous observations in the literature and extends

---

*Email addresses:* `ancrebo@mot.upv.es` (A. Cremades), `rvinuesa@mech.kth.se` (R. Vinuesa)

them by quantifying the importance of the Reynolds-stress structures, finding a causal connection between these structures and the dynamics of the flow. The process, based on deep-learning explainability, has the potential to shed light on numerous fundamental phenomena of wall-bounded turbulence, including the objective definition of new types of flow structures.

*Keywords:* Turbulence, Deep learning, Machine learning, Shapley values, Explainability, Coherent structures

---

## Introduction

Approximately 140 years ago, Osborne Reynolds published the first and most influential scientific article on turbulent flows [1]. One of the main conclusions of this study was the fact that the Navier–Stokes equations, which describe the behavior of any flow, can only be solved analytically for elementary flow configurations. For nearly a century, the study of turbulence has relied on experimental measurements [2–4] and theoretical considerations [5]. Almost all flows of practical interest are turbulent, except those relevant to lubrication [6]. In fact, one of the most crucial challenges nowadays, namely the current climate emergency, is closely connected with turbulence and a better understanding of the dynamics of turbulent flows is necessary to reduce greenhouse-gas and pollutant emissions. Approximately 30% of the energy consumption worldwide is used for transportation [7], which, due to the increase in drag caused by turbulent flow, is a problem very closely connected with wall-bounded turbulence. Furthermore, turbulence is critical in combustion processes [8, 9] and aerodynamics [10, 11]. It is also essential in energy generation [12, 13] or urban pollution [14, 15], to name just a few. In-

deed, some estimations indicate that 15% of the energy consumed worldwide is spent near the boundaries of vehicles and is therefore related to turbulent effects [16].

The main challenge is the fact that turbulence is a multi-scale phenomenon in both time and space. The energy is mainly transferred from the largest to the smallest scales of the flow, where it is dissipated [5], although there is also an energy path in the opposite direction [17]. There are several orders of magnitude between these scales for any flow in engineering. In the presence of a wall this energy cascade is even more complicated due to the energy and momentum transfer from the wall to the outer flow [18]. This multi-scale behavior implies that integrating numerically the Navier–Stokes equations requires extremely fine computational meshes leading to a prohibitive computational effort for practical applications.

In the 1980s, supercomputers became powerful enough to integrate these equations numerically in some canonical geometries. Kim et al. [19] simulated the simplest complete example of a wall-bounded flow, *i.e.*, a turbulent channel. They performed a direct numerical simulation (DNS), where all the spatial and temporal scales of the flow are resolved. Note that in DNS there are no additional hypotheses beyond the fact that the flow is governed by the Navier–Stokes equations. This numerical technique provides a complete flow characterization, and almost any imaginable quantity can be computed. Thus, DNS can provide a large amount of high-quality data, and simulations in the Petabyte scale are becoming progressively more common [20]. This enables fully characterizing the kinematics of wall-bounded turbulent flows. However, describing the dynamics of turbulent flows is still an open

challenge, as we are still many years away from applying DNS techniques to practical problems. It is then essential to develop novel methods to solve the questions posed 140 years ago.

One of the most successful ideas for studying turbulent flows focuses on the relationship among the different scales and coherent structures of the flow [18, 21]. Note that different definitions of coherent structure have been proposed in the literature. The first examples of coherent structure are the streamwise streaks [3] and the Reynolds-stress quadrants [22], which were first observed experimentally. The latter, also called intense Reynolds-stress events or  $Q$  events, are the object of our work. Coherent  $Q$  structures are flow regions associated with momentum transfer and turbulent-kinetic-energy (TKE) production. Two particular  $Q$  events defined below, ejections and sweeps, are the main contributors to the exchange of streamwise momentum. This process is the main energy source for all the structures present in turbulent flows [22, 23].  $Q$  events are also responsible for the generation of turbulent drag. Even with extensive studies on the contribution of the various coherent structures to the dynamics of turbulent flows, a clear understanding of their actual role still needs to be provided [18].

This study proposes a new technique for the study of wall-bounded turbulence. We have developed a novel methodology based on explainable artificial intelligence (XAI) to gain a more profound knowledge of the flow physics and to evaluate the contributions of the  $Q$  events to flow-field prediction. The methodology employs deep convolutional neural networks (CNNs) [24] and the Shapley additive explanation (SHAP) values [25–27]. CNNs can effectively extract the spatial information in the flow data [28], both in two and

three dimensions. The SHAP algorithm is a game-theoretic method that calculates the importance of each input feature on the CNNs prediction. SHAP has been shown to correctly identify key aspects of the near-wall cycle that sustains turbulence close to onset [29]. Thus, the main novelty of this work is the explainability of fully-developed turbulence through artificial intelligence. We calculate the relative importance of each Q event for the CNN prediction through SHAP. In doing so, we identify, in a purely data-driven method (without any hypothesis about the physics of the flow), relevant physical processes governing the dynamics of wall-bounded turbulence.

To accomplish this objective, we will first show how CNNs can predict the evolution of turbulent channel flow, as documented in our earlier work [30]. We start with a database of 4,900 instantaneous realizations of the channel flow; 60% of the fields are used for training and validation, while the rest are utilized for testing. For every field, the domain is segmented into Q events (see Methods section), and each one of these structures is considered an input feature to the SHAP algorithm. SHAP ranks the importance of each structure for predicting the following flow field, as shown schematically in Figure 1. This workflow consists of three main stages: prediction of the flow through a CNN, determination of the structure evolution (advance a time step in the simulation), and quantification of the importance of each coherent turbulent structure using SHAP values (and SHAP values per unit of volume) comparing the predicted solution with the simulated flow field in the next time step. By analyzing the characteristics of the highest-ranked structures, we can shed light on the dynamics of wall-bounded turbulence, with direct implications on the questions described above. We find coherent structures

representing ejections, where fluid volumes with low streamwise velocity move from the near-wall towards the outer region; and sweeps, where fluid volumes with high streamwise velocity move from the outer region towards the wall. Note that these are most important for the prediction of the flow. Our study confirms the results obtained by other authors [18, 31], introducing the usage of XAI to analyze turbulent flows and finding a causal connection between sweeps/ejections and the dynamics of the flow.

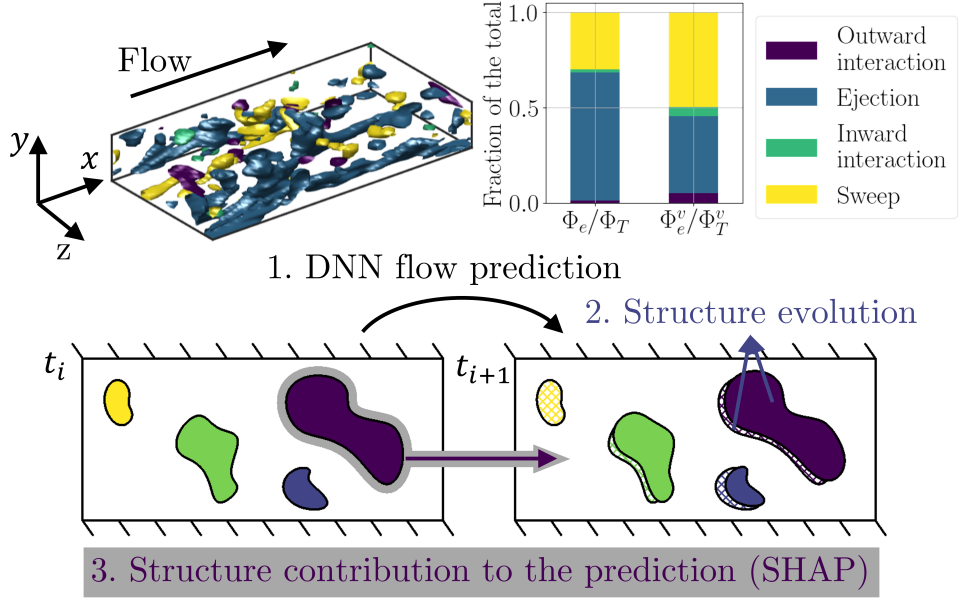


Figure 1: **Conceptual map of the workflow employed in this study.** (Top-left) Instantaneous Reynolds-stress ( $Q$ ) events identified in a turbulent channel. Four different kinds of structures exist based on the quadrant analysis [32]: outward interactions (purple), ejections (blue), inward interactions (green) and sweeps (yellow). (Top-right) Total contribution,  $\Phi_e/\Phi_T$ , (left column) and total contribution per unit volume,  $\Phi_e^v/\Phi_T^v$ , (right column) of each event type to the CNN prediction. Their definition and implications are discussed in the Results section. (Bottom) Workflow comprising three steps: 1) a CNN is used to predict the next instantaneous flow field (time  $t_{i+1}$ ) based on the current one ( $t_i$ ); 2) the structures evolve, so some may dissipate in the next field (yellow), others may be convected (rest of colors), and some may even merge into larger ones (not shown); 3) calculation of the contribution of each structure (gray shade) to the prediction of the next field. The error on the prediction of the flow field of the CNN in  $t_i$  with respect to the simulated flow in  $t_{i+1}$  is used to determine the importance of every single structure. In this way, it is possible to rank the various structures in terms of their relative importance to predict the next instantaneous field. The workflow is performed on the full three-dimensional data but shown on a vertical slice of the turbulent channel here for simplicity.

## Results

The geometry of a turbulent channel flow comprises two parallel planes at a distance of  $2h$ . A pressure gradient drives the flow along the channel. The spatial coordinates are  $x$ ,  $y$ , and  $z$ , in the streamwise, wall-normal, and spanwise directions, respectively. The length and width of the channel are  $L_x = 2\pi h$ , and  $L_z = \pi h$ , with streamwise and spanwise periodicity. This computational box is large enough to recover all the statistical information of the flow [32, 33].

The velocity vector is  $\mathbf{U}(x, y, z, t) = (U, V, W)$ , where  $t$  denotes time. As the flow is fully developed, its statistical information only depends on  $y$  [6]. Statistically-averaged quantities in  $x$ ,  $z$ , and  $t$  are denoted by an overbar, whereas fluctuating quantities are denoted by lowercase letters, *i.e.*,  $U = \overline{U} + u$ . Primes are reserved for root-mean-squared (rms) quantities:  $u' = \sqrt{\overline{u^2}}$ , which constitute a measure of the standard deviation from the mean flow.

The simulation was carried out at a friction Reynolds number  $Re_\tau = u_\tau h / \nu = 125$ . Note that  $\nu$  is the fluid kinematic viscosity and  $u_\tau = \sqrt{\tau_w / \rho}$  is the friction velocity ( $\tau_w$  is the wall-shear stress and  $\rho$  the fluid density) [6], while  $Re_\tau$  is the main control parameter. The value of  $Re_\tau$  attainable in numerical simulations has been increasing steadily in the last 35 years due to the advances in computational power and numerical methods [19, 20, 34–39]. Quantities nondimensionalized with the viscous scales  $u_\tau$  and  $\nu$  are denoted with a ‘+’ superscript. Finally, as the channel is statistically symmetric, the upper half-channel statistics are projected symmetrically onto the coordinates of the lower half.

The Q events are coherent regions of instantaneous high Reynolds stress, defined by:

$$|u(x, y, z, t)v(x, y, z, t)| > Hu'(y)v'(y). \quad (1)$$

In this equation,  $H$  is the so-called hyperbolic hole, set to a value of 1.75 [31]. Intuitively, equation (1) identifies the region where the instantaneous value of the Reynolds stress (the left-hand-side) is considerably larger than the product of the standard deviation of both  $u$  and  $v$ . Q events identify regions that have statistically large magnitudes of Reynolds stress. Based on the classical quadrant analysis [22, 31], four types of events can be defined: outward interactions ( $u > 0, v > 0$ ), structures with a high streamwise velocity that move from the wall to the bulk; ejections ( $u < 0, v > 0$ ), structures with a low streamwise velocity which move from the wall to the bulk; inward interactions ( $u < 0, v < 0$ ), structures with low streamwise velocity moving from the bulk to the wall; and sweeps ( $u > 0, v < 0$ ), structures with high streamwise velocity moving from the bulk to the wall, see Figures 1 and 3.

#### *Prediction of the velocity field*

As discussed in the Methods section, a CNN is trained to predict the evolution of the velocity field. The predictive capabilities of the CNN are assessed through the test database, which was not seen by the neural network during training. The quality of the prediction can be observed in Figure 2, where we show a slice of the instantaneous norm of the velocity vector from the reference simulation (top), the CNN prediction (middle), and their difference (bottom). The results show the high accuracy of the neural-network

prediction. As shown in Figure 2, the simulated and predicted flow fields are nearly identical. The larger differences appear in few grid points as the CNN slightly displaces some flow patterns without affecting the global prediction of the velocity field. The mean error between the simulation and the prediction averaged over the whole test database is  $0.47u_\tau$ , and the maximum error is  $2.33u_\tau$ . These correspond to 3.5% and 15% of the bulk velocity ( $U_b = 13.42u_\tau$ ), respectively. Part of these deviations are due to the fact that the CNN uses a mesh coarser than that of the simulation. Note that the employed resolution is sufficient for this study [29] and the reported errors are acceptable in the context of coherent-structure analysis.

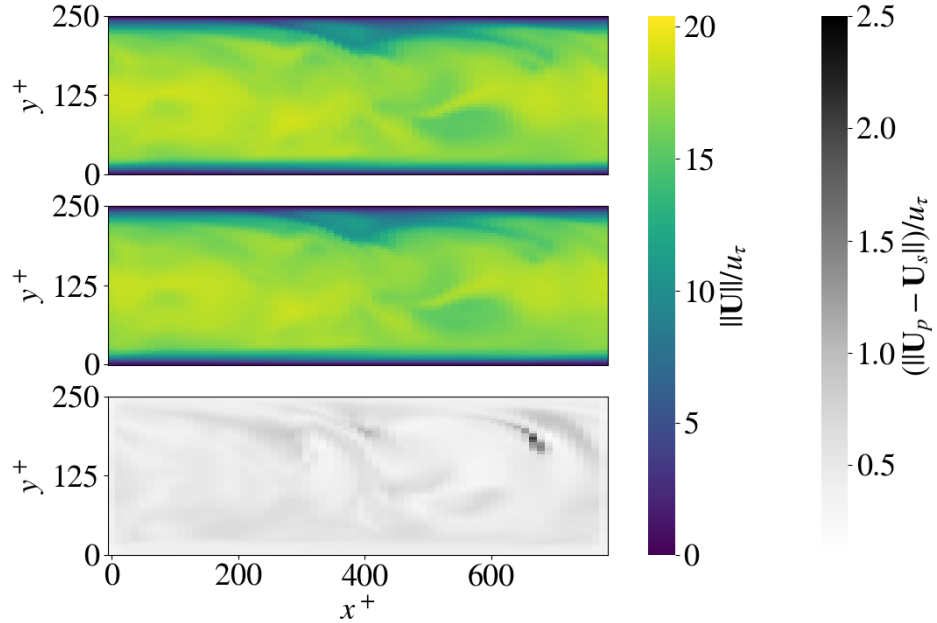


Figure 2: **Comparison of ground truth and prediction of a representative vertical slice at a single instance in time.** (Top) reference velocity field, (middle) predicted velocity field and (bottom) norm of the difference between the two previous fields, with a mean-squared error of  $0.47u_\tau$  averaged over the whole database. The subscripts  $s$  and  $p$  correspond to the fields in the reference simulation and the prediction, respectively.

#### Explainability of the CNN predictions

The CNN is used for calculating the contribution, based on the SHAP values [25, 40, 41], of the different turbulent structures to the prediction. A deeper explanation of how the SHAP values are used for assessing the importance of each Q event is discussed in the Methods section. The total importance of each typology of Q event,  $\Phi_e$ , is calculated by summing up the value of every structure belonging to this class of event,  $\phi_i^e$ , where  $i$  indicates a single coherent structure. The total contribution of all events, *i.e.* the

summation of all the SHAP values, is denoted by  $\Phi_T$ . Paraticularizing to a single class  $e$  (ejections, sweeps, outward or inward interactions), we can define the percentual importance of this class,  $\Phi_e/\Phi_T$ . For this particular application,  $\phi_i^e$  is always negative. The larger its absolute value, the more critical the structure is to reconstruct the field. In the context of this study, we will use the term *importance* to refer to this impact. The quantification of  $\phi_i^e$  for every structure can be used to evaluate their contribution to the turbulent flow. Moreover, this magnitude may be evaluated per unit volume, *i.e.* a SHAP density can be calculated. In this case, a different distribution of relative importance is obtained, identifying highly-important localized structures. The percentual importance per unit of volume is defined as:

$$\Phi_e^v = \sum_{i=1}^{I_e} \left( \frac{\phi_i}{V_i^+} \right)^e, \quad \Phi_T^v = \sum_{e=1}^4 \Phi_e^v, \quad (2)$$

where  $I_e$  is the number of structures of type  $e$  and  $(\phi_i/V_i^+)^e$  is the SHAP value per unit of volume of the structures type  $e$ . To avoid spurious results, we filtered out all volumes lower than  $V^+ = 10^4$  [31], which corresponds to 0.01% of the total volume of the channel.

In Figure 3 we can see an example of the flow and the relative importance of each structure. A wide variety of structures are present in the flow (top row, subfigures A). Turbulence is transported in self-contained bursts composed of sweep/ejection pairs, which generate streaks as a result [18, 31, 42]. This idea, which was previously proposed by Wallace et al. [23] and Lu and Willmarth [22], was further analysed by Lozano-Durán et al. [31] using probability density functions of the intense Reynolds-stress structures. Using  $\phi_i^e$ , we can quantitatively measure the importance of every single structure.

Complementing this, we can quantify the importance of every Q class. The total SHAP is presented in the top-right bar plot of Figure 1. In absolute terms, ejections are the most important events, as they represent 67.2% of the total contribution. They are followed by sweeps, with 30.0%. Inward and outward interactions account for the rest, as expected [18, 43]. To put these percentages in perspective, approximately 60% of the total number of structures in a turbulent channel are either sweeps or ejections [18]. The SHAP analysis associates the total number of sweeps and ejections with over 97% of the total SHAP or importance on the prediction, reinforcing the idea that the momentum transport relies on the self-contained bursts or ejection/sweep pairs. As shown in Figure 1, ejections are the largest structures. The size of ejections can also be appreciated in the slices A2) and B2) of Figure 3. Using the SHAP density (2), the percentual contribution of each type of structure is modified, being the sweeps the most influential structures per unit of volume (49.5%), with a similar contribution by the ejections (40.5%). Due to their small volume, the inward and outward interactions are not negligible, with approximately 5% of the total contribution each. However, this is still small compared with ejections and sweeps.

Furthermore, two different families of structures are observed [44]: wall attached, in which the lowest point is located at  $y^+ < 20$  (Figure 3, B2), and wall detached, in which the lowest point is located at  $y^+ \geq 20$  (Figure 3, A1). As stated by Lozano-Durán et al. [31] and Jiménez [18], the most important structures are the large ejections attached to the wall as they transport most of the Reynolds stress. To further analyse this situation, the SHAP value of the structures has been represented as a function of their volume, Fig-

ure 4 (left). Wall-attached ejections are confirmed as the most important structures, and sweeps have an undoubtly smaller value. This asymmetry between sweeps and ejections has been known since the work of Nakagawa and Nezu [45] and has also been discussed by many authors, see Ref. [18]. Lozano-Durán et al. [31] estimated that the Reynolds stress associated with the sweeps is weaker than that of the ejections. However, the data presented in Figure 4 shows that the most influential structures per unit of volume are the wall-attached sweeps. This is an important result, as it confirms the theory of the self-contained burst, ejection/sweep pair [42]. Although sweeps are smaller and have a lower impact than the ejections on the global flow field, their specific impact per unit volume on the solution is much higher than that of the large ejection. This configuration can be observed in the lateral view of the channel in Figure 3. The large ejections are located along the streamwise direction. These structures are parallel to the high-influence-per-volume wall-attached sweeps, which are located sequentially in the streamwise direction. In other words, the turbulence information is contained equally in the volume occupied by ejections and sweeps.

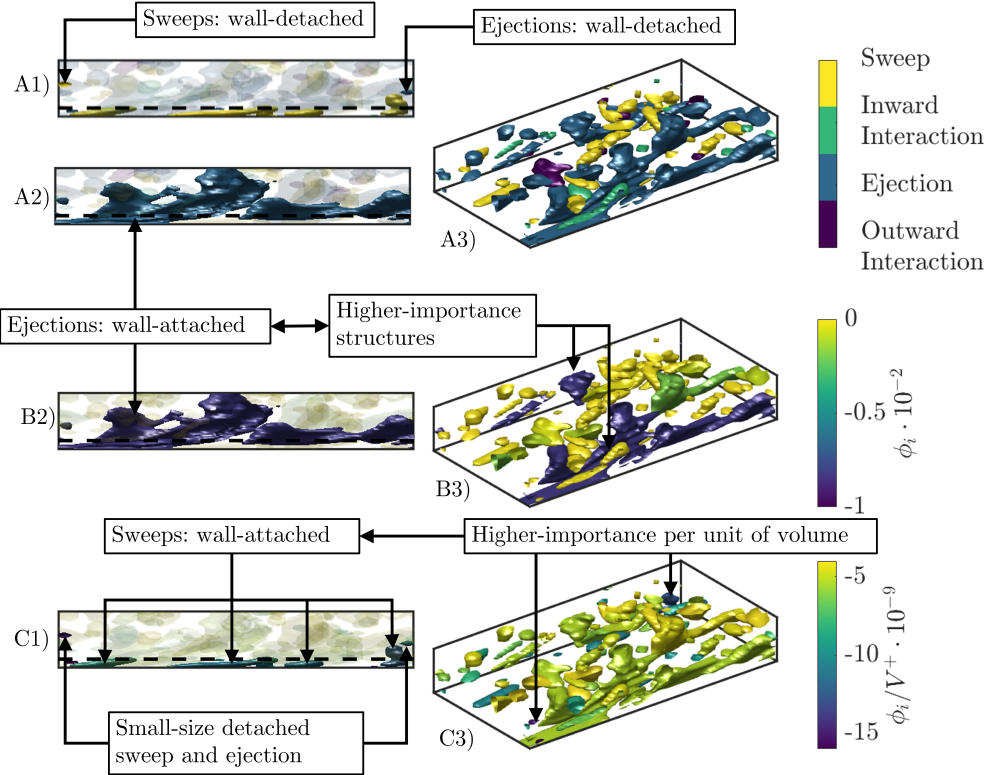


Figure 3: **Instantaneous visualization of the turbulent structures.** This Figure shows (views A) the type of turbulent structure, (views B) the SHAP values, and (views C) the SHAP values divided by the volume of the corresponding structures. The three-dimensional perspective is presented in images A3, B3, and C3. The side view of the turbulent channel (left) highlights the more influential structures (views A2 and B2). The most important structures per unit of volume are highlighted in views A1 and C1. Note that the highest SHAP values are obtained for large wall-attached ejections, while the wall-attached sweeps exhibit the highest influence per unit of volume. The dashed line marks  $y^+ = 20$ , which was used in the previous studies [31] to separate wall-attached and wall-detached structures. The visualization is presented for half of the channel in all the subfigures.

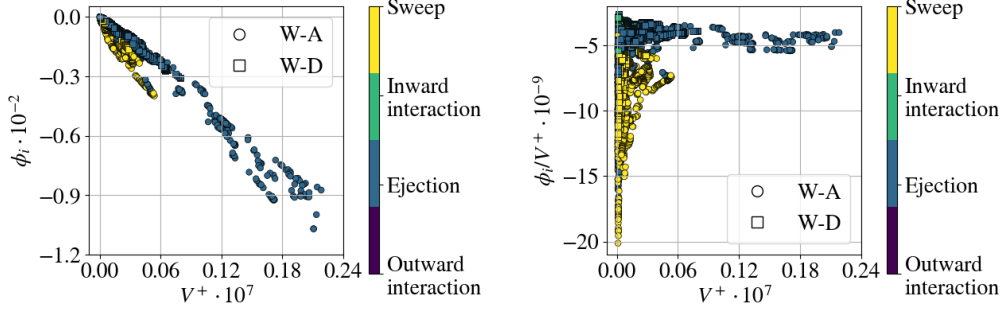


Figure 4: **SHAP values (left)** and **SHAP values per unit of volume (right)** of the structures for different turbulent events as a function of their volume. The SHAP values determine the importance of the various turbulent structures, *i.e.* the most relevant structures exhibit a higher modulus of the SHAP value. Ejections are the most important structures for the predictions, while sweeps exhibit a higher value per unit volume. Wall-attached structures exhibit higher SHAP values and SHAP values per unit of volume than wall-detached. In addition, outward and inward interactions, which have a negligible volume, exhibit low SHAP values in absolute terms. While larger structures exhibit a high SHAP value, the smaller structures have a larger SHAP value per unit volume.

The method proposed in this work has so far confirmed the current state of the art regarding Q events. However, it is important to assess whether the SHAP framework simply quantifies the Reynolds-stress contribution of each structure or it performs a more nuanced analysis. In order to address this point, we compute the total Reynolds stress from each structure  $\bar{uv}_{\text{tot}}$ , defined as:

$$\bar{uv}_{\text{tot}} = \int_e u(x, y, z)v(x, y, z)d\mathbf{x}, \quad (3)$$

where the integration is done for every structure  $e$  and  $\mathbf{x}$  is the spatial-

coordinate vector. Without taking into account the volume, see Figure 5 (left), there exists a clear correlation between  $\bar{uv}_{\text{tot}}$  and the SHAP values. The more Reynolds stress the structure carries, the larger its SHAP is. However, when scaling the SHAP and  $\bar{uv}_{\text{tot}}$  distributions by the volume, the results are very different as shown in Figure 5 (right): the correlation between these two quantities disappears. High-SHAP-density sweeps are the most important ones, together with some wall-attached ejections and wall-detached sweeps. This figure confirms that the SHAP framework not only offers a complete quantification of the structures but is also different from simply quantifying the Reynolds stresses associated with the structures.

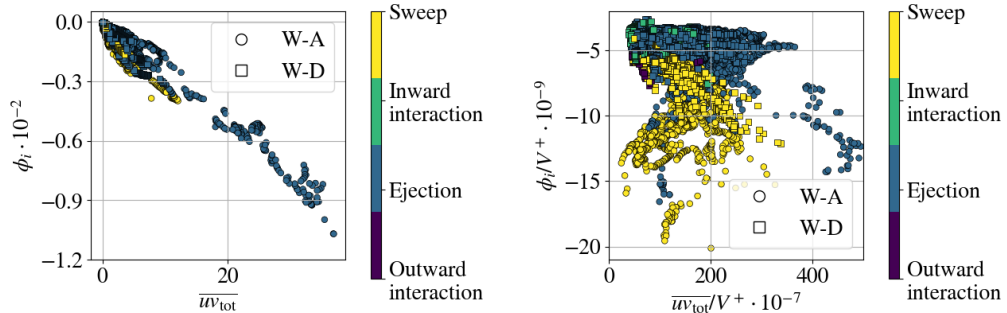


Figure 5: **SHAP values for the tangential Reynolds stress (left) and SHAP values per unit of volume for the tangential Reynolds stress per unit of volume (right).** A clear relationship between the SHAP values and the Reynolds stress appears in the left panel. However, this is an effect of the size of the structures. The SHAP and total-Reynolds-stress densities in the right panel exhibit a different behavior: the correlation disappears, and the wall-attached sweeps become the most important structures.

To further confirm these results, the relative importance of every structure has been quantified by calculating the normalized kernel-density estimation

(KDE) of the SHAP values and the SHAP values per unit of volume, shown in Figure 6. Again, the ejection/sweep pair is the most influential structure. In addition, ejections are more important than sweeps in absolute terms. However, the importance of the type of event changes using the volumetric SHAP. In this case, the influence of the sweeps is higher than that of the ejections, and the outward and inward interactions are not negligible due to their low volume. However, they still contribute significantly less to the prediction than ejections and sweeps do, as previously presented in Figure 1.

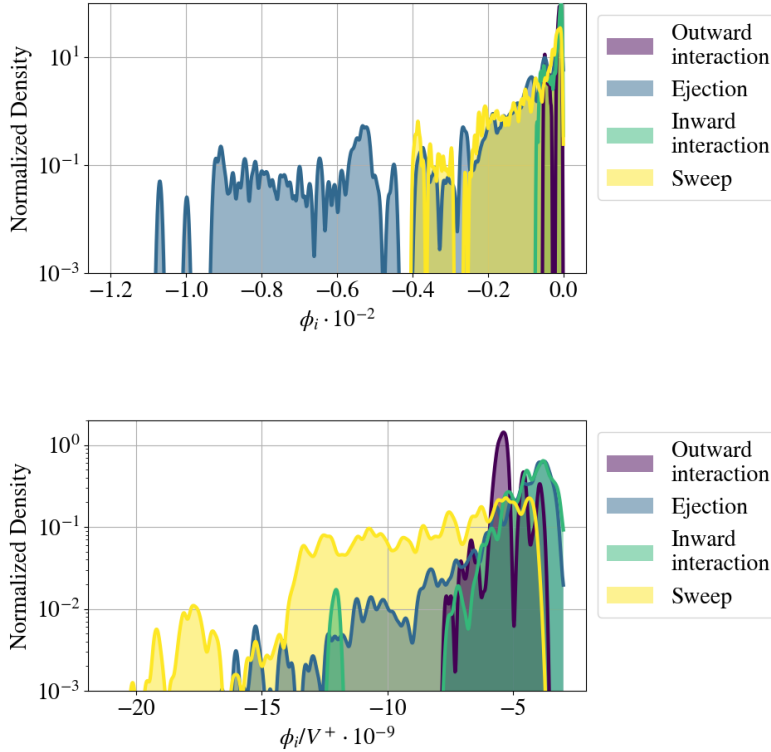


Figure 6: **Normalized kernel-density estimation (KDE) of the SHAP values (top) and the SHAP values per unit of volume (bottom) for the different coherent structures.** KDE represents a smooth normalized point-centered block histogram of the various events. The present results are based on using a Gaussian kernel function for smoothing the estimation and the bandwidth is selected via cross-validation.

Regarding the shape of the dominant structures, Figure 7 shows the SHAP value of ejections and sweeps as a function of the aspect ratio of the structures. The aspect ratios are measured on the bounding box of each structure, being  $\Delta x$ ,  $\Delta y$ , and  $\Delta z$  are the streamwise, wall-normal, and spanwise dimensions of the box, respectively. As stated by Lozano-Durán et al.

[31] and Jiménez [42], the most important structures are large wall-attached ejections, followed by wall-attached sweeps. These structures are expected to exhibit [31] an aspect ratio of  $\Delta x \approx 3\Delta y$  and  $\Delta z \approx \Delta y$ . These results were obtained for a higher Reynolds number, and the present methodology yields similar results ( $3\Delta y < \Delta x < 6\Delta y$ ) for the principal structures. Note that these coherent structures, *i.e.* the wall-attached structures, are elongated in the streamwise direction [46]. In addition, these results confirm the idea proposed by Jiménez [18], namely that the coherent structures (streamwise momentum transfer) are generated as a result of the shear, not of the wall, which is demonstrated by the spanwise aspect ratio  $\Delta z \approx \Delta y$ . Furthermore, the Q events of high volume and importance, which cross the central plane, exhibit a relationship between the spanwise and wall-normal directions closer to  $\Delta z \approx 1.5\Delta y$ , as previously reported in Ref. [44]. Note that the isotropic structures  $\Delta x \approx \Delta y$  are negligible for predicting turbulent flow due to their small size. These structures are decoupled from the shear and form the local Kolmogorov inertial range [18]. Apart from the previous analysis, the most significant structures per unit volume are around seven times larger in the streamwise direction than in the normal-wall direction ( $\Delta x \approx 7\Delta y$ ) and of similar sizes in the spanwise and normal-wall directions ( $\Delta z \approx \Delta y$ ). This fact shows that the more elongated a structure is, the higher influence per unit of volume it has on the turbulent flow. The most elongated structures are wall-attached sweeps, as shown in view A1) of Figure 3. Therefore, for turbulence models, the correct calculation of elongated structures is demonstrated to be crucial.

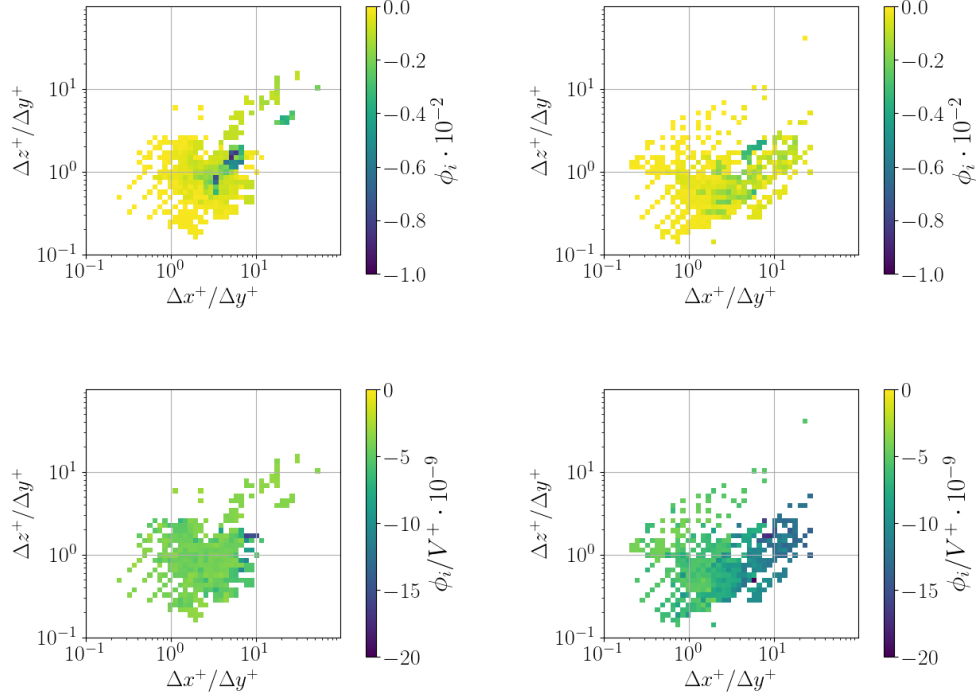


Figure 7: **SHAP values (top)** and **SHAP values per unit of volume (bottom)** of the ejections (left) and the sweeps (right) for the sizes of the boxes circumscribing the Reynolds-stress structures. Note that here we focus on the aspect ratio of the boxes, and the most important structures are located below the  $\Delta z^+/\Delta y^+ = \Delta x^+/\Delta y^+$  diagonal. Consequently, these structures exhibit values of  $\Delta z^+$  lower than those of  $\Delta x^+$ . The most important structures for the predictions are elongated in the streamwise direction.

Finally, the points not belonging to any structure are irrelevant for the energy transfer [31, 43]. To show that, every point not belonging to any Q event has been merged into a single background structure. The absolute SHAP of this structure is negligible compared with the SHAP of the Q events, even if this one is by far the largest structure of the flow.

Note that these results, obtained in a purely data-driven manner, are in excellent agreement with those by Jiménez [18], Lozano-Durán et al. [31], a fact that confirms the potential of the present framework to discover relevant trends in turbulence data. Firstly, the wall-attached structures have been demonstrated to carry most of the tangential Reynolds stress. These wall-attached structures are mainly ejections and sweeps, being outward and inward interactions negligible for turbulence prediction. In addition, the large ejections which extend along the whole channel concentrate most of the tangential Reynolds stress. With respect to the aspect ratio of the main structures, they are in the range  $3 < \Delta x / \Delta y \leq 6$  and  $\Delta z / \Delta y \approx 1$ .

In addition, the explainable-CNN methodology also provides information about the importance per unit volume of the coherent structures. Relative to this point of view, wall-attached sweeps are the most important structures. In this case, the aspect ratio of the main structures is bigger than in the case of the absolute SHAP value  $\Delta x \approx 7\Delta y$ , demonstrating that the influence per unit volume of the structures is directly related to their elongation. Finally, the total contribution per unit of volume of both ejections and sweeps compensates as they both form coherent pairs which transport the shear stress.

## Discussion and conclusions

This article uses XAI to predict the importance of intense Reynolds-stress structures. Sweeps and ejections are shown to be the most relevant structures for fully-developed turbulence in a channel. This fact was stated by Lozano-Durán et al. [31], but in this work, the previous knowledge is confirmed

with a purely data-driven methodology that can be easily adapted to more complicated flows. These computational tools were used for quantifying, for the first time, the relative importance concerning turbulent dynamics of each intense Reynolds-stress structure in the flow. The structures were extracted from the simulation of a turbulent channel. They were used to segment the computational domain. Then, their importance on the flow was calculated by measuring their contribution to the CNN prediction.

The results show a high influence of two types of structures: ejections and sweeps. These structures are of high importance in the generation of turbulent self-contained bursts [18, 42] and are associated with turbulence production. When assessing the global prediction of the next instantaneous field, the higher-volume structures are the most influential. The larger structures correspond to wall-attached ejections, which extend through the channel, transporting a substantial fraction of the total Reynolds stress [32]. These ejections exhibit the most negative SHAP values (higher absolute value), meaning that their presence is essential for the correct prediction of the CNN. However, when analyzing the influence of the structure relative to its volume, different trends are obtained. In this case, the most influential structures per unit of volume are the wall-attach sweeps, which pair with the ejections.

Relative to the shape of the structures, the most influential structures per unit of volume exhibit larger aspect ratios in the streamwise direction than in the spanwise direction. In addition, the wall-normal direction is around 3 to 6 times smaller for the higher-SHAP structures and 7 times smaller for the higher SHAP-per-unit-volume structures. These facts demonstrate that the more elongated the structure is, the higher its influence on turbulence.

The framework presented here has enabled, in a purely data-driven manner, to confirm and expand some of the basic knowledge of wall-bounded turbulence available in the literature [18, 31]. Here we can obtain an objective quantification of the importance of various types of coherent flow structures, finding a causal connection between sweeps/ejections and the dynamics of the flow. Future work will aim at objectively identifying other types of coherent structures, shedding light on the fundamental phenomena of wall-bounded turbulence. In terms of turbulence modeling, a similar approach may be taken to first quantify and subsequently understand the significance of coherent structures, and of dynamical processes such as vortex stretching and strain amplification in data-driven subgrid-scale representations, for instance, when based on invariants of the velocity-gradient tensor. Furthermore, the present methodology shows the potential of using explainable deep learning for turbulence control [47] and, thus, for the reduction of energy consumption in transportation.

## Methods

### *Numerical simulations and flow case under study*

The CNN was trained using 4,900 instantaneous velocity fields obtained through DNS. The simulations are calculated in a box with periodic boundaries confined between two parallel plates and driven by an imposed pressure gradient. The employed code is LISO [48], which has been used to run some of the largest simulations of wall-bounded turbulence [20]. The convergence of the turbulence statistics was assessed based on the criterion of linear total shear [49]. The data obtained with LISO has been extensively validated

against experimental and other numerical studies [36, 50] and is broadly used [51–53].

#### *Deep-neural-network architecture and prediction*

A convolutional neural network (CNN) is used for predicting the velocity field, as discussed by Schmekel et al. [30]. Note that CNNs and other computer-vision architectures have been successfully used in the context of turbulent-flow predictions [28, 54–57]. The convolution operation is described by Equation (4), where  $f$  is the input three-dimensional (3D) tensor,  $h$  the filter,  $G$  the output, and  $m$ ,  $n$  and  $p$  the indices of the output tensor:

$$G(m, n, p) = (f * h)(m, n, p) = \sum_i \sum_j \sum_k h(i, j, k) f(m - i, n - j, p - k). \quad (4)$$

The network employed in this work consists of 4 layers of 3D CNN blocks, which contain plain convolutional and residual blocks [58]. The architecture, similar to the one used by Schmekel et al. [30], is shown in Figure 8. Each convolution comprises a total of 16 filters with size  $5 \times 3 \times 5$ , where the number of layers and filters of the model were selected to obtain adequate accuracy with an optimum computational cost. The network uses a total of 65,135 parameters (where 99.8% of them are trainable). The network input consists of 3D volumes with  $67 \times 64 \times 64$  grid points corresponding to downsampled instantaneous flow fields, which originally contain  $201 \times 96 \times 192$  grid points. Here, 60% of the flow fields are used for the training-and-validation process (out of which 80% are used for training and 20% for validation). Rectified-linear-unit (ReLU) activation functions are used for the hidden layers due to their low computational cost and the reduction of the vanishing-gradients problem [59]. Nevertheless, a sigmoid function is

used for the output layer to obtain a smooth normalized output. For this process, an RMSprop optimizer is used [60]. The remaining 40% of fields are reserved for testing and explainability analysis, and are not seen by the network during training. The training process is concluded when the mean-square-error-based loss function is lower than  $10^{-4}$ , corresponding to  $1.5 \times 10^4$  epochs, where all training data is used once in a single epoch.

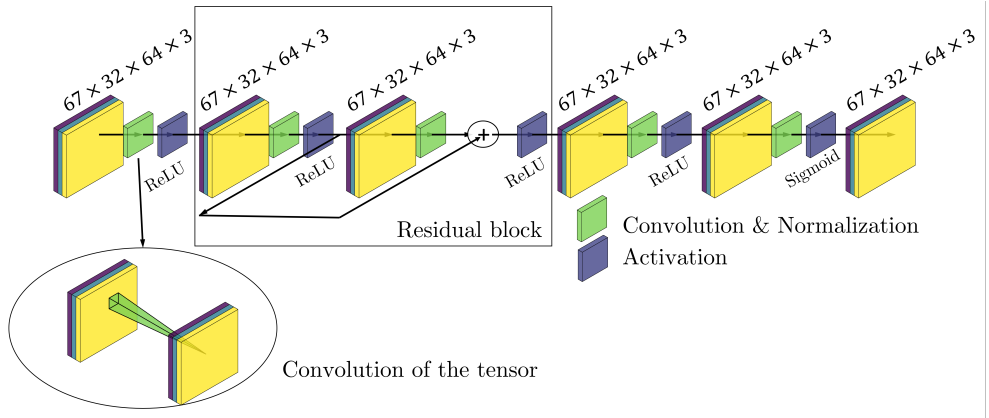


Figure 8: **Schematic architecture of the convolutional neural network.** (Top) Architecture of the CNN including convolutional and residual blocks. The various activation functions, namely the rectified linear unit (ReLU) and the sigmoid, are also shown. (Bottom) Simplified schematic of the convolution operation.

#### *Explainability of the neural network*

Despite the excellent results achieved with deep learning, the relationships between inputs and outputs are complex, and it is, in general, challenging to explain the predictions based on a particular input field. The SHAP framework [25] is used to evaluate the contribution of each feature (coherent structure in this case) to the prediction of the next flow field. In this work, the importance of the Reynolds-stress structures is of interest. Thus, a mask

function is defined to convert from the original space into the space of the structures. The importance is calculated as the influence that each structure has on the prediction by means of the SHAP-kernel method [25]. The workflow of this method is shown in Figure 9.

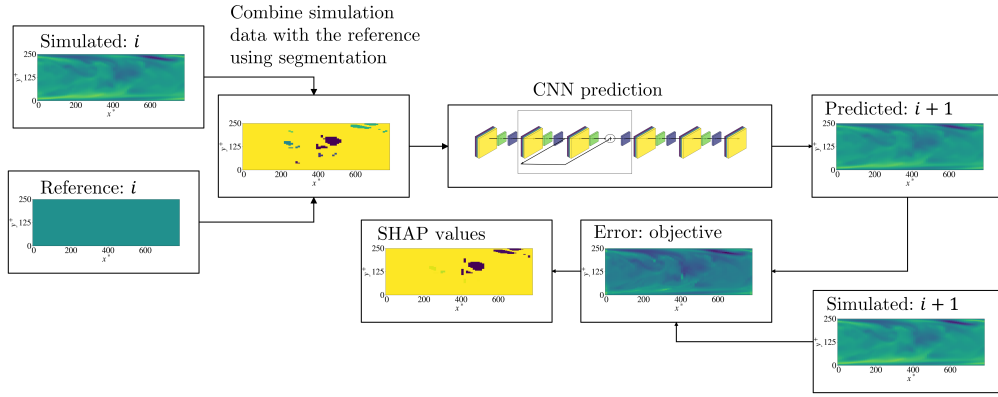


Figure 9: **Simplified SHAP-kernel algorithm.** The SHAP-kernel algorithm can be divided into different stages. In the first one, the domain is segmented. Then, the results are predicted using the CNN for each structure. The error between this prediction and the simulated solution is used to determine the SHAP value of each feature.

The SHAP-kernel method is based on two distinct components: LIME [61] and Shapley values, while the explanation value is represented as an additive feature attribution method. The SHAP values explain the CNN prediction as a sum of the marginal contributions of the input features through a linear-regression model:

$$g(q') = \phi_0 + \sum_{j=1}^{N_Q} \phi_j q'_j, \quad (5)$$

where  $g$  is the linear-regression function,  $\phi_0$  the reference output of  $g$ ,  $\phi_j$  the

SHAP values,  $q'_j$  the binary value of the input feature (coherent-structure presence: 1 if present and 0 if absent) and  $N_Q$  is the number of features. When a feature is absent, the grid points contained in the structure are substituted by the corresponding nodes in a reference matrix  $\mathbf{U}_r$ . In the present work, the reference is defined as a null velocity-fluctuation matrix to neglect the turbulence in the deleted Q events. Therefore, as the input of the CNN is a velocity-fluctuation matrix, the reference matrix contains all zeros:  $\mathbf{U}_r = [0]_{67 \times 32 \times 64 \times 3}$ . The SHAP values are optimized by reducing the mean-squared-error loss function, which is given as follows for the training data  $Q'$ :

$$\mathcal{L}(\hat{f}, g, \pi_x) = \sum_{q' \in Q'} \left[ \hat{f}(h_x(q')) - g(q') \right]^2 \pi_x(q'), \quad (6)$$

where the squared error of each  $q'$  is obtained by calculating the difference between the error of the CNN model with respect to the simulation,  $\hat{f}$ , and the linear model,  $g$ . To obtain these predictions, the features must be mapped, through the function  $h_x$ , to assign each feature of the  $q'$  vector to the group of grid points corresponding to the coherent structure. The contribution of each feature to the predictions,  $\pi_x$ , is calculated as follows, where  $|q'|$  is the number of present features:

$$\pi_x(q') = \frac{N_Q - 1}{\binom{N_Q}{|q'|} |q'| (N_Q - |q'|)}. \quad (7)$$

Since the CNN provides a  $67 \times 32 \times 64 \times 3$  output tensor, an additional layer must be added to the neural-network model to obtain a single output

to calculate the function  $\hat{f}$ . Thus, the objective function to evaluate is the mean-squared error of the three velocity components in each field, which is given by:

$$\hat{f}(h_x(q')) = \frac{\sum_{ijkl} \sqrt{(\mathbf{U}_{s_{ijkl}} - \mathbf{U}_{p_{ijkl}}(h_x(q')))^2}}{67 \times 32 \times 64 \times 3}, \quad (8)$$

where  $s$  and  $p$  denote data from the original simulation and the CNN prediction, respectively.

Due to the fact that the reference tensor neglects the velocity fluctuations, the reference value of the error (*i.e.* the error when the prediction of the reference matrix is evaluated) is higher than the error when any  $Q$  (feature) is included. This definition has two important consequences: first, the prediction error is lower when the reference values are used in the areas with low-velocity fluctuation (background structure), as they are similar to the reference matrix; thus, these features are expected to exhibit a lower SHAP value. Second, as including the structures will reduce the mean error concerning the reference, all the SHAP values should be negative. Finally, it is also important to note that in the present application the SHAP value quantifies the modification that including a feature produces in the prediction error. In this case, neglecting the velocity fluctuation of the whole computational domain produces the highest prediction error. Therefore, the SHAP values are negative and including a feature (coherent structure) reduces this error. Consequently, the importance of each feature is determined by its modulus.

## Acknowledgments

This project has been partially funded by the Spanish Ministry of Science, Innovation, and University through the University Faculty Training (FPU) program with reference FPU19/02201 (AC). The data has been obtained with support of grant PID2021-128676OB-I00 funded by MCIN/AEI/10.13039/501100011033 and by “ERDF A way of making Europe”, by the European Union (SH). RV acknowledges the financial support from ERC grant no. ‘2021-CoG-101043998, DEEPCONTROL’. Views and opinions expressed are however those of the author(s) only and do not necessarily reflect those of the European Union or the European Research Council. Neither the European Union nor the granting authority can be held responsible for them.

## Author Contributions

**Cremades, A.:** Methodology, Software, Validation, Investigation, Writing - Original Draft, Visualization **Hoyas, S.:** Data curation, resources, Writing - Original Draft, Funding acquisition **Quintero, P.:** Writing - Review & Editing, Funding acquisition **Linkmann, M** Writing - Review & Editing **Lellep, M.** Writing - Review & Editing **Vinuesa, R.:** Conceptualization, project definition, methodology, resources, Writing - Review & Editing, Supervision, Project administration, Funding acquisition.

## Data availability

The data and codes used to produce this study will be made available for open access as soon as the article is published.

## References

- [1] O. Reynolds, An experimental investigation of the circumstances which determine whether the motion of water shall be direct or sinuous, and of the law of resistance in parallel channels, *Philosophical Transactions of the Royal society of London* 174 (1883) 935–982.
- [2] G. I. Taylor, The spectrum of turbulence, *Proceedings of the Royal Society of London. Series A - Mathematical and Physical Sciences* 164 (1938) 476–490. doi:10.1098/rspa.1938.0032.
- [3] S. J. Kline, W. C. Reynolds, F. A. Schraub, P. W. Runstadler, The structure of turbulent boundary layers, *Journal of Fluid Mechanics* 30 (1967) 741–773. doi:10.1017/S0022112067001740.
- [4] A. Townsend, *The Structure of Turbulent Shear Flows*, 2nd ed., Cambridge University Press, New York,, 1976.
- [5] A. N. Kolmogorov, Local structure of turbulence in an incompressible fluid at very high Reynolds numbers., *Dokl. Akad. Nauk. SSSR* (30) (1941) 9–13.
- [6] S. B. Pope, *Turbulent flows*, Cambridge University Press, 2000.
- [7] I. E. Agency, Key world energy statistics, <https://www.iea.org/reports/key-world-energy-statistics-2020>, accessed 20-nov-2022, IEA, Paris, 2020.
- [8] A. R. Kerstein, Turbulence in combustion processes: modeling challenges, *Proceedings of the Combustion Institute* 29 (2002) 1763–1773.

- [9] N. Peters, Multiscale combustion and turbulence, *Proceedings of the Combustion Institute* 32 (2009) 1–25.
- [10] P. Panagiotou, K. Yakinthos, Aerodynamic efficiency and performance enhancement of fixed-wing UAVs, *Aerospace Science and Technology* 99 (2020) 105575.
- [11] R. Vinuesa, O. Lehmkuhl, A. Lozano-Durán, J. Rabault, Flow Control in Wings and Discovery of Novel Approaches via Deep Reinforcement Learning, *Fluids* 7 (2022) 62.
- [12] W. D. Lubitz, Impact of ambient turbulence on performance of a small wind turbine, *Renewable Energy* 61 (2014) 69–73.
- [13] M. Optis, J. Perr-Sauer, The importance of atmospheric turbulence and stability in machine-learning models of wind farm power production, *Renewable and Sustainable Energy Reviews* 112 (2019) 27–41.
- [14] A. G. Ulke, M. F. Andrade, Modeling urban air pollution in São Paulo, Bazil: sensitivity of model predicted concentrations to different turbulence parameterizations, *Atmospheric environment* 35 (2001) 1747–1763.
- [15] E. Solazzo, X. Cai, S. Vardoulakis, Modeling wind flow and vehicle-induced turbulence in urban streets, *Atmospheric environment* 42 (2008) 4918–4931.
- [16] J. Jiménez, Near-wall turbulence, *Physics of Fluids* 25 (2013) 101302.
- [17] J. I. Cardesa, A. Vela-Martín, J. Jiménez, The turbulent cascade in five dimensions, *Science* 357 (2017) 782–784.

- [18] J. Jiménez, Coherent structures in wall-bounded turbulence, *Journal of Fluid Mechanics* 842 (2018) P1.
- [19] J. Kim, P. Moin, R. Moser, Turbulence statistics in fully developed channels flows at low Reynolds numbers, *Journal of Fluid Mechanics* 177 (1987) 133–166.
- [20] S. Hoyas, M. Oberlack, F. Alcántara-Ávila, S. V. Kraheberger, J. Laux, Wall turbulence at high friction Reynolds numbers, *Physical Review Fluids* 7 (2022) 014602. doi:10.1103/PhysRevFluids.7.014602.
- [21] J. I. Cardesa, A. Vela-Martín, J. Jiménez, The turbulent cascade in five dimensions, *Science* 357 (2017) 782–784.
- [22] S. S. Lu, W. W. Willmarth, Measurements of the structure of the Reynolds stress in a turbulent boundary layer, *Journal of Fluid Mechanics* 60 (1973) 481–511. doi:10.1017/S0022112073000315.
- [23] J. M. Wallace, H. Eckelmann, R. S. Brodkey, The wall region in turbulent shear flow, *Journal of Fluid Mechanics* 54 (1972) 39–48. doi:10.1017/S0022112072000515.
- [24] Y. LeCun, Y. Bengio, G. Hinton, Deep learning, *Nature* 521 (2015) 436–444.
- [25] S. M. Lundberg, S.-I. Lee, A unified approach to interpreting model predictions, *Advances in neural information processing systems* 30 (2017).
- [26] Y. Meng, N. Yang, Z. Qian, G. Zhang, What Makes an Online Review More Helpful: An Interpretation Framework Using XGBoost and

SHAP Values, Journal of Theoretical and Applied Electronic Commerce Research 16(3) (2021) 466–490.

- [27] S. Lun-Chau, R. Hu, J. Gonzalez, D. Sejdinovic, RKHS-SHAP: Shapley Values for Kernel Methods, Preprint arXiv:2110.09167v2 (2022).
- [28] L. Guastoni, A. Güemes, A. Ianiro, S. Discetti, P. Schlatter, H. Azizpour, R. Vinuesa, Convolutional-network models to predict wall-bounded turbulence from wall quantities, Journal of Fluid Mechanics 928 (2021) A27. doi:10.1017/jfm.2021.812.
- [29] M. Lellep, J. Prexl, B. Eckhardt, M. Linkmann, Interpreted machine learning in fluid dynamics: explaining relaminarisation events in wall-bounded shear flows, Journal of Fluid Mechanics 942 (2022) A2.
- [30] D. Schmekel, F. Alcántara-Ávila, S. Hoyas, R. Vinuesa, Predicting coherent turbulent structures via deep learning, Frontiers in Physics 10 (2022) 888832.
- [31] A. Lozano-Durán, O. Flores, J. Jiménez, The three-dimensional structure of momentum transfer in turbulent channels, Journal of Fluid Mechanics 694 (2012) 100–130.
- [32] A. Lozano-Durán, J. Jiménez, Effect of the computational domain on direct simulations of the turbulent channels up to  $Re_\tau = 4200$ , Physics of Fluids 26 (2014) 011702.
- [33] F. Lluesma-Rodríguez, S. Hoyas, M. Pérez-Quiles, Influence of the computational domain on dns of turbulent heat transfer up to  $Re_\tau = 2000$

for  $Pr = 0.71$ , International journal of heat and mass transfer 122 (2018) 983–992.

- [34] R. Moser, J. Kim, N. Mansour, Direct numerical simulation of turbulent channel flow up to  $Re_\tau = 590$ , Physics of Fluids 11 (1999) 943–945.
- [35] J. Del Alamo, J. Jiménez, P. Zandonade, R. Moser, Scaling of the energy spectra of turbulent channels, Journal of Fluid Mechanics 500 (2004) 135–144.
- [36] S. Hoyas, J. Jiménez, Scaling of the velocity fluctuations in turbulent channels up to  $Re_\tau = 2003$ , Physics of Fluids 18 (2006) 011702.
- [37] M. Bernardini, S. Pirozzoli, P. Orlandi, Velocity statistics in turbulent channel flow up to  $Re_\tau = 4000$ , Journal of Fluid Mechanics 758 (2014) 327–343.
- [38] M. Lee, R. Moser, Direct numerical simulation of turbulent channel flow up to  $Re_\tau \approx 5200$ , Journal of Fluid Mechanics 774 (2015) 395–415.
- [39] Y. Yamamoto, Y. Tsuji, Numerical evidence of logarithmic regions in channel flow at  $Re_\tau = 8000$ , Physical Review Fluids 3 (2018) 012602(R).
- [40] G. Fidel, R. Bitton, A. Shabtai, When explainability meets adversarial learning: Detecting adversarial examples using shap signatures, in: 2020 International Joint Conference on Neural Networks (IJCNN), 2020, pp. 1–8. doi:10.1109/IJCNN48605.2020.9207637.
- [41] J. V. Jeyakumar, J. Noor, Y.-H. Cheng, L. Garcia, M. Srivastava, How can i explain this to you? an empirical study of deep neural network ex-

planation methods, Advances in Neural Information Processing Systems 33 (2020) 4211–4222.

- [42] J. Jiménez, The streaks of wall-bounded turbulence need not be long, *Journal of Fluid Mechanics* 945 (2022) R3. doi:10.1017/jfm.2022.572.
- [43] B. Ganapathisubramani, E. K. Longmire, I. Marusic, Characteristics of vortex packets in turbulent boundary layers, *Journal of Fluid Mechanics* 478 (2003) 35–46.
- [44] J. C. del Álamo, J. Jiménez, P. Zandonade, R. Moser, Self-similar vortex clusters in the turbulent logarythmic region, *Journal of Fluid Mechanics* 561 (2006) 329–358.
- [45] H. Nakagawa, I. Nezu, Prediction of the contributions to the Reynolds stress from bursting events in open-channel flows, *Journal of Fluid Mechanics* 80 (1977) 99–128. doi:10.1017/S0022112077001554.
- [46] S. Dong, A. Lozano-Durán, A. Sekimoto, J. Jiménez, Coherent structures in statistically stationary homogeneous shear turbulence, *Journal of Fluid Mechanics* 816 (2017) 167–208. doi:10.1017/jfm.2017.78.
- [47] L. Guastoni, J. Rabault, P. Schlatter, H. Azizpour, R. Vinuesa, Deep reinforcement learning for turbulent drag reduction in channel flows, Preprint arXiv:2301.09889 (2023).
- [48] F. Lluesma-Rodríguez, F. Álcantara Ávila, M. Pérez-Quiles, S. Hoyas, A code for simulating heat transfer in turbulent channel flow, *Mathematics* 9 (2021). doi:10.3390/math9070756.

- [49] R. Vinuesa, C. Prus, P. Schlatter, H. Nagib, Convergence of numerical simulations of turbulent wall-bounded flows and mean cross-flow structure of rectangular ducts, *Meccanica* 51 (2016) 3025–3042.
- [50] S. Hoyas, J. Jiménez, Reynolds number effects on the Reynolds-stress budgets in turbulent channels, *Physics of Fluids* 20 (2008) 101511.
- [51] P. Monkewitz, The late start of the mean velocity overlap log law at a generic feature of turbulent wall layers in ducts, *Journal of Fluid Mechanics* 910 (2021). doi:10.1017/jfm.2020.998.
- [52] P. Spalart, H. Abe, Empirical scaling laws for wall-bounded turbulence deduced from direct numerical simulations, *Physical Review Fluids* 6 (2021). doi:10.1103/PhysRevFluids.6.044604.
- [53] S. Pirozzoli, J. Romero, M. Fatica, R. Verzicco, P. Orlandi, DNS of passive scalars in turbulent pipe flow, *Journal of Fluid Mechanics* 940 (2022).
- [54] A. Güemes, S. Discetti, A. Ianiro, B. Sirmacek, H. Azizpour, R. Vinuesa, From coarse wall measurements to turbulent velocity fields through deep learning, *Physics of Fluids* 33 (2021) 075121.
- [55] L. Yu, M. Z. Yousif, M. Zhang, S. Hoyas, R. Vinuesa, H. C. Lim, Three-dimensional ESRGAN for super-resolution reconstruction of turbulent flows with tricubic interpolation-based transfer learning, *Physics of Fluids* 34 (2022) 125126.
- [56] M. Z. Yousif, L. Yu, S. Hoyas, R. Vinuesa, H. C. Lim, A deep-learning

approach for reconstructing 3D turbulent flows from 2D observation data, Preprint arXiv:2208.05754 (2022).

- [57] M. Z. Yousif, M. Zhang, L. Yu, R. Vinuesa, H. C. Lim, A transformer-based synthetic-inflow generator for spatially-developing turbulent boundary layers, *Journal of Fluid Mechanics*, To Appear. Preprint arXiv:2208.05754 (2022).
- [58] K. He, X. Zhang, S. Ren, J. Sun, Deep residual learning for image recognition, In: *Proceedings of the IEEE conference on computer vision and pattern recognition*, 2016, pp. 770–778.
- [59] H. H. Tan, K. H. Lim, Vanishing gradient mitigation with deep learning neural network optimization, in: *2019 7th international conference on smart computing & communications (ICSCC)*, IEEE, 2019, pp. 1–4.
- [60] F. Zou, L. Shen, Z. Jie, W. Zhang, W. Liu, A sufficient condition for convergences of Adam and RMSProp, in: *Proceedings of the IEEE/CVF Conference on computer vision and pattern recognition*, 2019, pp. 11127–11135.
- [61] M. T. Ribeiro, S. Singh, C. Guestrin, Why Should I Trust You? Explaining the Predictions of Any Classifier, In *Proceedings of the 22nd ACM SIGKDD International Conference on Knowledge Discovery and Data Mining*, 2016, pp. 1135–1144.